

Machine-learning-assisted efficient reconstruction of the quantum states generated from the Sagnac polarization-entangled photon source

Menghui Mao(毛梦辉), Wei Zhou(周唯), Xinhui Li(李新慧), Ran Yang(杨然), Yan-Xiao Gong(龚彦晓), and Shi-Ning Zhu(祝世宁)

Citation: Chin. Phys. B, 2024, 33 (**8**): 080301. DOI: 10.1088/1674-1056/ad51f7
Journal homepage: http://cpb.iphy.ac.cn; http://iopscience.iop.org/cpb

What follows is a list of articles you may be interested in

Recurrent neural network decoding of rotated surface codes based on distributed strategy

Fan Li(李帆), Ao-Qing Li(李熬庆), Qi-Di Gan(甘启迪), and Hong-Yang Ma(马鸿洋)
Chin. Phys. B, 2024, 33 (**4**): 040307. DOI: 10.1088/1674-1056/ad2bef

Analysis of learnability of a novel hybrid quantum—classical convolutional neural network in image classification

Tao Cheng(程涛), Run-Sheng Zhao(赵润盛), Shuang Wang(王爽), Rui Wang(王睿), and Hong-Yang Ma(马鸿洋)
Chin. Phys. B, 2024, 33 (**4**): 040303. DOI: 10.1088/1674-1056/ad1926

Deep learning framework for time series classification based on multiple imaging and hybrid quantum neural networks

Jianshe Xie(谢建设) and Yumin Dong(董玉民)
Chin. Phys. B, 2023, 32 (**12**): 120302. DOI: 10.1088/1674-1056/accb45

Variational quantum semi-supervised classifier based on label propagation

Yan-Yan Hou(侯艳艳), Jian Li(李剑), Xiu-Bo Chen(陈秀波), and Chong-Qiang Ye(叶崇强)
Chin. Phys. B, 2023, 32 (**7**): 070309. DOI: 10.1088/1674-1056/acb9fb

A new method of constructing adversarial examples for quantum variational circuits

Jinge Yan(颜金歌), Lili Yan(闫丽丽), and Shibin Zhang(张仕斌)
Chin. Phys. B, 2023, 32 (**7**): 070304. DOI: 10.1088/1674-1056/ac9b32

SPECIAL TOPIC — Quantum communication and quantum network

Machine-learning-assisted efficient reconstruction of the quantum states generated from the Sagnac polarization-entangled photon source

Menghui Mao(毛梦辉)[†], Wei Zhou(周唯)[†], Xinhui Li(李新慧), Ran Yang(杨然), Yan-Xiao Gong(龚彦晓)[‡], and Shi-Ning Zhu(祝世宁)

National Laboratory of Solid State Microstructures and School of Physics, Nanjing University, Nanjing 210093, *China*

(Received 11 May 2024; revised manuscript received 29 May 2024; accepted manuscript online 30 May 2024)

Neural networks are becoming ubiquitous in various areas of physics as a successful machine learning (ML) technique for addressing different tasks. Based on ML technique, we propose and experimentally demonstrate an efficient method for state reconstruction of the widely used Sagnac polarization-entangled photon source. By properly modeling the target states, a multi-output fully connected neural network is well trained using only six of the sixteen measurement bases in standard tomography technique, and hence our method reduces the resource consumption without loss of accuracy. We demonstrate the ability of the neural network to predict state parameters with a high precision by using both simulated and experimental data. Explicitly, the mean absolute error for all the parameters is below 0.05 for the simulated data and a mean fidelity of 0.99 is achieved for experimentally generated states. Our method could be generalized to estimate other kinds of states, as well as other quantum information tasks.

Keywords: machine learning, state estimation, quantum state tomography, polarization-entangled photon source

PACS: 03.65.Ud, 03.65.Wj, 02.60.–x, 42.50.Dv **DOI:** 10.1088/1674-1056/ad51f7

1. Introduction

With the development of quantum technologies, the technique of producing quantum entangled states has become increasingly widespread and mature, finding various applications in quantum information tasks, such as quantum teleportation,[1–4] quantum random number generation,[5–7] and quantum computation.[8–10] The canonical method to characterize a quantum state is the technique of quantum state tomography[11,12] (QST), which allows one to reconstruct the density matrix of a quantum state through local measurements. However, such method is resource-intensive, requiring extensive time and computational resources for the full reconstruction of the state in practical experiments. The efficient characterization of quantum entangled states remains an unresolved problem.

On the other hand, machine learning (ML) is a branch of artificial intelligence (AI) that focuses on the development of algorithms and models capable of learning from data to make predictions or decisions. Over the past decades, machine learning has increasingly been used in various fields of physics for solving diverse tasks,[13,14] such as particle physics,[15] astronomy,[16] material sciences.[17] In recent years, machine learning has been demonstrated as a novel and efficient platform for solving problems in quantum information science,[18] such as classification of quantum entangled states,[19–21] estimation of quantum states,[22–24] and development of novel algorithms for solving many-body systems.[25]

In this work, we aim to exploit machine learning to reduce the resource consumption for reconstructing the entangled states generated from a widely used polarization-entangled photon source employing a type-Ⅱ phase-matched periodically poled crystal pumped in two directions in a Sagnac interferometer.[26–28] Such kind of source has the merits of high brightness, high-quality with intrinsic phase stability, and thus shows broad prospects in the verification of the basic principles of quantum mechanics,[29–32] quantum communication,[33–35] and quantum computation.[36,37] We first establish a model for experimentally generated entangled states. Then we train a multi-output fully connected neural network (FCNN) using simulated data from only six of the sixteen measurement bases in standard tomography technique. Note that the FCNN is a prominent example of supervised learning algorithms with interconnected layers of neurons fully connected to the next,[38,39] enabling the network to learn complex mappings from input features to output predictions through its hidden layers. We demonstrate the performance of the well-trained FCNN using both simulated and experimental data. Theoretically, we achieve a negligible mean error of below 0.05 for all relevant parameters with simulated input data. Experimentally, we characterize a series of states and obtain an average fidelity of 0.99. These results demon-

[†]These authors contributed equally to this work.

[‡]Corresponding author. E-mail: gongyanxiao@nju.edu.cn

© 2024 Chinese Physical Society and IOP Publishing Ltd

strate the validity and efficiency of the machine learning assisted state reconstruction scheme.

2. Modelling the target state

We first give a brief description of the polarization-entangled photon source with Sagnac interferometer and analyze possible noises and imperfections. Then we present a model that accurately describes these states which are then utilized as the training set for the FCNN.

The structure of the polarization-entangled photon source is shown in Fig. 1. The Sagnac interferometer is composed of a polarization beam splitter (PBS), a half-wave plate (HWP_2), two high-reflection mirrors (M), and a periodically poled potassium titanyl phosphate (PPKTP) crystal that is designed for satisfying the type-Ⅱ quasi-phase-matching condition for spontaneous parametric down-conversion (SPDC) process. The PBS and HWP_2 are fabricated with antireflection coating for both pump and down-converted wavelengths. The pump light directed into the interferometer is split at the PBS with the horizontal and vertical components traveling clockwise and counterclockwise, respectively. Frequency-degenerated polarization-orthogonal SPDC photon pairs are generated from PPKTP in two directions. HWP_2 is set at $\pi/4$ to rotate the pump and the photon pairs. Then the two-direction photon pairs are combined at the PBS, resulting in the polarization entangled state $\alpha|H\rangle_A|V\rangle_B + \beta|V\rangle_A|H\rangle_B$, where the subscripts A and B refer to the two output ports of the PBS. The coefficients α and β originate from the polarization of the pump light $\alpha|H\rangle + \beta|V\rangle$, which are controlled by HWP_1 and a quarter-wave plate (QWP_1). When the pump polarization is adjust to the ideal case $(|H\rangle - |V\rangle)/\sqrt{2}$, the maximally entangled state $|\Psi^-\rangle = (|H\rangle_A|V\rangle_B - |V\rangle_A|H\rangle_B)/\sqrt{2}$ can be generated.

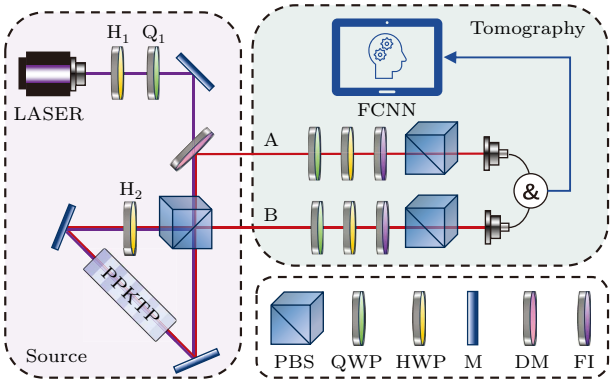


Fig. 1. Schematic of the polarization-entangled photon source with Sagnac interferometer and measurement setups in tomography stage. PPKTP: periodically poled potassium titanyl phosphate crystal, PBS: polarization beam splitter, QWP: quarter-wave plate, HWP: half-wave plate, M: high reflecting mirror, DM: dichromic mirror, FI: bandpass filter.

Then we analyze possible noises and imperfections of the state in practical experiment. The main contamination to the ideal state results from the imperfection in the interferometer loop, which may induce imbalance and dephasing noise between $|H\rangle_A|V\rangle_B$ and $|V\rangle_A|H\rangle_B$ terms. In addition, the deviation in polarization elements could bring inherent white noises. Hence, the state is then modeled as follows:

$$\rho_m(t,s,\lambda) = \frac{1}{1+t}\left(\frac{|\psi\rangle\langle\psi| + sI\otimes I}{1+4s} + t|\Psi^+\rangle\langle\Psi^+|\right), \quad (1)$$

where $|\psi\rangle = \lambda|H\rangle_A|V\rangle_B - \sqrt{1-\lambda^2}|V\rangle_A|H\rangle_B$ with $\lambda \in [0,1]$. The decoherence is expressed by adding a proportion of another type of Bell state $|\Psi^+\rangle = (|H\rangle_A|V\rangle_B + |V\rangle_A|H\rangle_B)/\sqrt{2}$ to the density matrix and I is the identity matrix representing the white noises. This model is highly consistent with experiential observations from typical experiments.[26,27] Consequently, the task of reconstructing the density matrix is transformed into the estimation of three real parameters $\{t,\ s,\ \lambda\}$.

For the sake of reference, we calculate fidelities between the density matrix of some experimentally generated states and the ones generated through our model in Eq. (1). The average fidelity reaches 0.993, revealing the fact that the theoretically generated entangled states are closely aligned with the experimentally generated ones. Therefore, the theoretical data can serve as a reliable substitute for training the FCNN.

3. Training and testing of the FCNN

We aim to reconstruct the density matrix of the target state using only part of the measurement results of the QST. The choice of measurement configurations has a substantial impact on the performance of the FCNN and requires thorough consideration. For this purpose, we first do basis decomposition of the target state given by Eq. (1) as

$$\begin{aligned}\rho_m = \frac{1}{1+t}\Bigg[&\left(\frac{s+1}{1+4s}+\frac{t}{4}\right)I_A\otimes I_B \\ &+\frac{2\lambda^2-1}{4(1+4s)}(Z_A\otimes I_B - I_A\otimes Z_B) \\ &-\left(\frac{1}{1+4s}-\frac{t}{4}\right)Z_A\otimes Z_B \\ &+\frac{1}{2}\left(\frac{t}{2}-\frac{\lambda\sqrt{1-\lambda^2}}{1+4s}\right)(X_A\otimes X_B + Y_A\otimes Y_B)\Bigg], \quad (2)\end{aligned}$$

where I, X, Y, Z denote the Pauli operators with respect to the polarization basis. Based on the above decomposition we choose the measurement bases $\{II,\ IZ,\ ZI,\ XX,\ YY,\ ZZ\}$ as the input to estimate the parameters $\{t,\ s,\ \lambda\}$.

Since there are multiple target variables to be estimated, a multi-output regression is required, which is an important task in machine learning. In contrast to the standard regression where a single value is predicted for each sample, multi-output regression requires specialized machine learning algorithms that support outputting multiple variables for each prediction. As shown in Fig. 3, the FCNN is designed to address the multi-output regression task. It consists of an input layer,

five hidden layers, and two output layers connected to three output neurons, each corresponding to a different target variable t, s and λ, respectively.

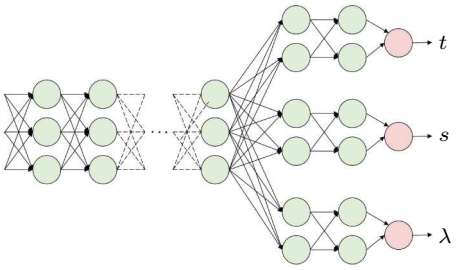


Fig. 2. The structure of the FCNN includes the input layer, hidden layer, and output layer.

The FCNN is trained using a set of loss functions corresponding to each output. Typically, the overall loss L for the network can be a weighted sum of individual loss functions for the targets t, s and λ,

$$L = \omega_t \cdot L_t + \omega_s \cdot L_s + \omega_\lambda \cdot L_\lambda, \tag{3}$$

where ω_t, ω_s, ω_λ are weights that balance the importance of each task. Since the ranges of these three parameters are identical, the weights can be defined as $\omega_t = \omega_s = \omega_\lambda = 1$. During training, gradient descent is used to minimize the loss function L. The gradients of L with respect to the weights of the network W are calculated as

$$\frac{\partial L}{\partial \boldsymbol{W}} = w_t \cdot \frac{\partial L_t}{\partial \boldsymbol{W}} + w_s \cdot \frac{\partial L_s}{\partial \boldsymbol{W}} + w_\lambda \cdot \frac{\partial L_\lambda}{\partial \boldsymbol{W}}. \tag{4}$$

These gradients are then used to update the weights of the network in the direction that reduces the loss, typically according to the rule

$$\boldsymbol{W}_{\text{new}} = \boldsymbol{W}_{\text{old}} - \eta \cdot \frac{\partial L}{\partial \boldsymbol{W}}, \tag{5}$$

where η is the learning rate. This process is repeated iteratively over many epochs until the network performance converges to a satisfactory level or a predefined number of epochs is reached. Following the standard paradigm of statistical learning, a dataset consisting of 100000 training samples with randomly generated t, s and λ is utilized to train the model parameters. According to the identical distribution assumption, the parameters are evenly distributed in $[0,1]$. We choose a large sample size in order to ensure the accuracy of model evaluation and to mitigate the risk of overfitting and model bias. In order to further improve the robustness, we employ the dropout method during the training process of our model.[40] Dropout means temporarily removing it from the network, along with all its incoming and outgoing connections. We randomly drop out 20% units in the neural work for each training iteration.

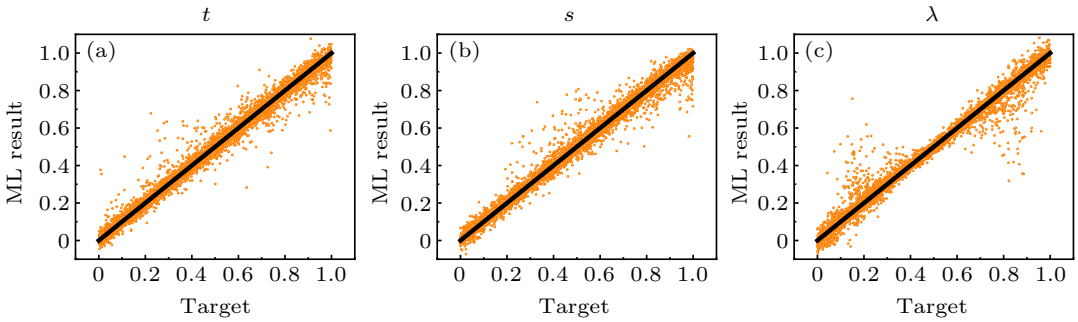


Fig. 3. Performance of the three parameters. The black line represents the theoretical value and the orange dots represent the prediction results.

After the model was well trained, the performance of the model was quantified using standard regression metrics by another 10000 testing samples. It can be evaluated by two indicators of mean absolute error (MAE) and mean squared error (MSE) given by

$$\text{MAE} = \frac{1}{n}\sum_{i=1}^{n}\left|Y_i - \hat{Y}_i\right|, \tag{6}$$

$$\text{MSE} = \frac{1}{n}\sum_{i=1}^{n}\left(Y_i - \hat{Y}_i\right)^2, \tag{7}$$

where Y_i is the actual value, and $\hat{Y}_i$ is the parameter predicted using machine learning, with n representing the total number of samples. The estimated results for the three parameters are depicted in Fig. 3. The MAE values for the three output parameters are 0.0262, 0.0265 and 0.0540, respectively, which indicate a close approximation of the predicted values to the actual ones. The MSE values are 0.0017, 0.0018, and 0.0105, respectively. These results suggest a high degree of accuracy and model reliability in predicting the targeted outputs as well as with low error margins.

4. Experimental demonstration of machine learning assisted reconstruction of quantum states

With the above test, we can employ the well-trained FCNN to reconstruct the state generated from the entangled photon source in a real experiment. In our experiment setup shown in Fig. 1, we use a 405-nm-wavelength continues-wave pump laser light to pump a 2-cm-long PPKTP crystal to gen-

erate polarization-entangled photon pairs centered at 810 nm. The source achieves a peak coincidence count rate of 7000 Hz at a pump power of 0.95 mW. During the tomography stage, a set of QWP, HWP and PBS is utilized to perform projection measurement at each side. Coincidence counts are obtained by single-photon detectors (SPDs) and a coincidence counter with a coincidence window of 500 ps and an integral time of 3 s. In total, we generate five distinct folds of quantum states that are close to the maximally entangled states.

Table 1. Comparison between the estimated parameters via machine learning (ML) and quantum state tomography (QST). The last column gives the fidelity between the ML-estimated and QST density matrices.

Number	t		s		λ		Fidelity
	QST	ML	QST	ML	QST	ML	
1	0.0000	0.0420	0.0002	0.0015	0.7044	0.6940	0.9806
2	0.0117	0.0055	0.0007	0.0025	0.7117	0.7010	0.9956
3	0.0045	0.0102	0.0041	0.0017	0.7250	0.7150	0.9919
4	0.0120	0.0112	0.0005	0.0005	0.7042	0.7150	0.9951
5	0.0120	0.0014	0.0000	0.0000	0.7176	0.6440	0.9857

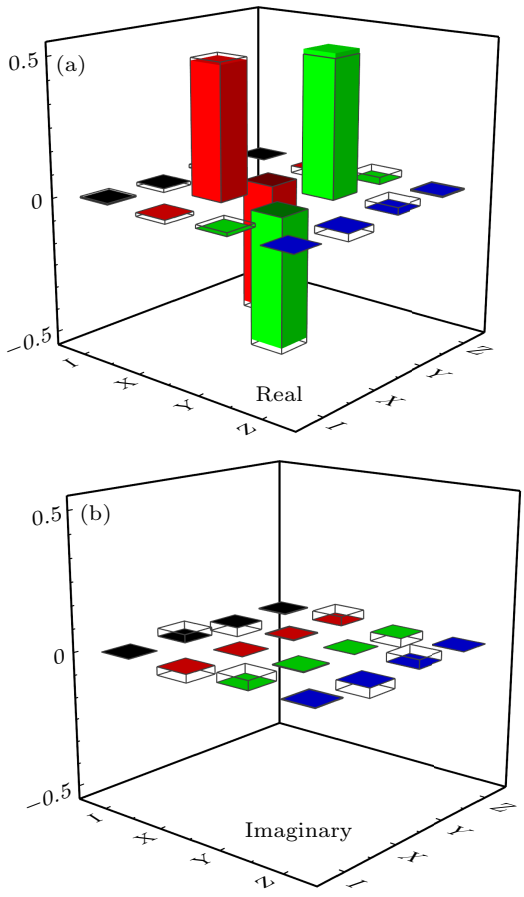


Fig. 4. Comparison of density matrices ρ_{QST} and ρ_{ML}. The density matrix obtained via QST is plotted with transparent background and black border while the one obtained via FCNNs is filled with color.

The predictive endeavor is conducted by inputting the results for the measurement configuration in Section 2 into the FCNN, thus instigating a forward propagation through the layers and returning a set of parameters $\{t_{\mathrm{ML}}, s_{\mathrm{ML}}, \lambda_{\mathrm{ML}}\}$ at the output layer. Substituting these parameters into Eq. (1), we can get the estimated density matrix ρ_{ML}. For the sake of reference, we do QST on each state and calculate the density matrix ρ_{QST}. The fidelity between the ML-estimated and QST density matrices is then calculated via $F(\rho_{\mathrm{ML}}, \rho_{\mathrm{QST}}) = \mathrm{Tr}\sqrt{\sqrt{\rho_{\mathrm{ML}}}\rho_{\mathrm{QST}}\sqrt{\rho_{\mathrm{ML}}}}$. Also, the parameters $\{t_{\mathrm{QST}}, s_{\mathrm{QST}}, \lambda_{\mathrm{QST}}\}$ are extracted from ρ_{QST} by maximizing the fidelity $F[\rho_{\mathrm{QST}}, \rho_{\mathrm{m}}(t_{\mathrm{QST}}, s_{\mathrm{QST}}, \lambda_{\mathrm{QST}})]$.

The resultant output values of the FCNN and their comparison against the values computed by QST are shown in Table 1.

The MAEs of the parameters t, s, and λ are 0.0131, 0.0010 and 0.0231, respectively. An average fidelity of 0.9900 across the five folds of states is achieved, indicating an accurate estimation of quantum states. Besides, a comparison of the density matrix obtained by QST and our FCNNs is presented in Fig. 3. Notably, despite the presence of nonzero terms particularly in the imaginary part of the density matrix, the density matrix reconstructed by our method closely resembles the QST matrix. The high prediction accuracy results demonstrate that the model has the ability to learn from training data to predict unknown datasets.

5. Conclusion

In conclusion, we proposed and experimentally demonstrated an efficient method to reconstruct the states generated from a widely used kind of polarization-entangled photon source with a Sagnac structure. The method is based on a machine learning algorithm that employs a multi-output FCNN trained with properly modeled states. With both simulated and experimental data, we demonstrated that the method can accurately reconstruct the entangled states by using only six of the sixteen measurement bases in standard tomography technique, thus greatly reducing the consumption of measurement resources.

Although our method is only capable of characterizing a specific kind of states, it can be straightforwardly generalized to the estimation of other kinds of states. Our method is an exploration of the combination of machine learning and quantum information. Our approach provides an evidence that machine learning is beneficial to solving problems in quantum information and also other scientific fields. We hope that our approach may stimulate more such investigations.

Acknowledgments

Project supported by the National Key Research and Development Program of China (Grant No. 2019YFA0705000), Leading-edge technology Program of Jiangsu Natural Science Foundation (Grant No. BK20192001), and the National Natural Science Foundation of China (Grant No. 11974178).

References

[1] Bennett C H, Brassard G, Crepeau C, Jozsa R, Peres A and Wootters We K 1993 *Phys. Rev. Lett.* **70** 1895
[2] Peters N A, Barreiro J T, Goggin M E, Wei T C and Kwiat P G 2005 *Phys. Rev. Lett.* **94** 150502
[3] Zhang Q, Goebel A, Wagenknecht C, Chen Y A, Zhao B, Yang T, Mair A, Schmiedmayer J and Pan J W 2006 *Nat. Phys.* **2** 678
[4] Liu X, Hu J, Li Z F, Li X, Li P Y, Liang P J, Zhou Z Q, Li C F and Guo G C 2021 *Nature* **594** 41
[5] Pironio S, Acin A, Massar S, de la Giroday A B, Matsukevich D N, Maunz P, Olmschenk S, Hayes D, Luo L, Manning T A and Monroe C 2010 *Nature* **464** 1021
[6] Christensen B G, McCusker K T, Altepeter J B, Calkins B, Gerrits T, Lita A E, Miller A, Shalm L K, Zhang Y, Nam S W, Brunner N, Lim C C W, Gisin N and Kwiat P G 2013 *Phys. Rev. Lett.* **111** 130406
[7] Liu W Z, Li M H, Ragy S, Zhao S R, Bai B, Liu Y, Brown P J, Zhang J, Colbeck R, Fan J, Zhang Q and Pan J W 2021 *Nat. Phys.* **17** 448
[8] Kok P, Munro W J, Nemoto K, Ralph T C, Dowling J P and Milburn G J 2007 *Rev. Mod. Phys.* **79** 135
[9] Ladd T D, Jelezko F, Laflamme R, Nakamura Y, Monroe C and O'Brien J L 2021 *Nature* **464** 45
[10] Knill E, Laflamme R and Milburn G J 2001 *Nature* **409** 46
[11] White A G, James D F V, Eberhard P H and Kwiat P G 1999 *Phys. Rev. Lett.* **83** 3103
[12] James D F V, Kwiat P G, Munro W J and White A G 2001 *Phys. Rev. A* **64** 052312
[13] Ma Y G, Pang L G, Wang R and Zhou K 2023 *Chin. Phys. Lett.* **40** 122101
[14] Suresh R, Bishnoi H, Kuklin A V, Parikh A, Molokeev M, Harinarayanan R, Gharat S and Hiba P 2024 *Front. Phys.* **12**
[15] Coelho C N, Kuusela A, Li S, Zhuang H, Ngadiuba J, Aarrestad T K, Loncar V, Pierini M, Pol A A and Summers S 2021 *Nat. Mach. Intell.* **3** 675
[16] Kremer J, Stensbo-Smidt K, Gieseke F, Pedersen K S and Igel C 2017 *IEEE Intelligent Systems* **32** 16
[17] Butler K T, Davies D W, Cartwright H, Isayev O and Walsh A 2017 *Nature* **559** 547
[18] Jiang W, Lu Z and Deng D L 2022 *Chin. Phys. Lett.* **39** 050303
[19] Gao J, Qiao L F, Jiao Z Q, Ma Y C, Hu C Q, Ren R J, Yang A L, Tang H, Yung M H and Jin X M 2018 *Phys. Rev. Lett.* **120** 240501
[20] Ma Y C and Yung M H 2018 *npj Quantum Inf.* **4** 34
[21] Yang M, Ren C, Ma Y, Xiao Y, Ye X J, Song L L, Xu J S, Yung M H, Li C F and Guo G C 2019 *Phys. Rev. Lett.* **123** 190401
[22] Ren C and Chen C 2019 *Phys. Rev. A* **100** 022314
[23] Zhang X, Luo M, Wen Z, Feng Q, Pang S, Luo W and Zhou X 2021 *Phys. Rev. Lett.* **127** 130503
[24] Koutný D, Ginés L, Moczaĺa-Dusanowska M, H´ofling S, Schneider C, Predojević A and Ježek M 2023 *Sci. Adv.* **9** 7131
[25] Carleo G and Troyer M 2017 *Science* **355** 602-6
[26] Sun Y, Sun C W, Zhou W, Yang R, Duan J C, Gong Y X, Xu P and Zhu S N 2023 *Chin. Phys. B* **32** 080308
[27] Fedrizzi A, Herbst T, Poppe A, Jennewein T and Zeilinger A 2007 *Opt. Express* **15** 15377
[28] Kim T, Fiorentino M and Wong F N C 2006 *Phys. Rev. A* **73** 012316
[29] Sun Q C, Jiang Y F, Bai B, Zhang W, Li H, Jiang X, Zhang J, You L, Chen X, Wang Z, Zhang Q, Fan J and Pan J W 2019 *Nat. Photonics* **13** 687
[30] Gómez S, Mattar A, Machuca I, Gómez E S, Cavalcanti D, Farías O J, Acín A and Lima G 2019 *Phys. Rev. A* **99** 032108
[31] Hu M J, Zhou Z Y, Hu X M, Li C F, Guo G C and Zhang Y S 2018 *npj Quantum Inf.* **4** 63
[32] Gómez E S, Gómez S, González P, Cañas G, Barra J F, Delgado A, Xavier G B, Cabello A, Kleinmann M, Vértesi T and Lima G 2016 *Phys. Rev. Lett.* **117** 260401
[33] Huang Y, Li Y, Qi Z, Yang Y, Zheng Y and Chen X 2023 *Quantum Front.* **2** 4
[34] Li J Y, Fang X X, Zhang T, Tabia G N M, Lu H and Liang Y C 2021 *Phys. Rev. Res.* **3** 023045
[35] Liu H Y, Tian X H, Gu C, Fan P, Ni X, Yang R, Zhang J N, Hu M, Guo J, Cao X, Hu X, Zhao G, Lu Y Q, Gong Y X, Xie Z and Zhu S N 2020 *Natl. Sci. Rev.* **7** 921
[36] Sun K, Hao Z Y, Wang Y, Li J K, Xu X Y, Xu J S, Han Y J, Li C F and Guo G C 2022 *Light Sci. Appl.* **11** 203
[37] Wu T, Izaac J A, Li Z-X, Wang K, Chen Z-Z, Zhu S, Wang J B and Ma X-S 2020 *Phys. Rev. Lett.* **125** 240501
[38] Hsu K Y, Li H Y and Psaltis D 1990 *Proc. IEEE* **78** 1637
[39] Lewenstein M and Nowak A 1990 *Phys. Rev. Lett.* **62** 225
[40] Srivastava N, Hinton G, Krizhevsky A, Sutskever I and Salakhutdinov R 2014 *Mach. Learn. Res.* **15** 1929